Chem. Soc. Faraday Trans. **82**, 2385 (1986).
9. For a review, see R. J. Hamers, *Annu. Rev. Phys. Chem.* **40**, 531 (1989).
10. F. Zuo, M. Angelopoulos, A. G. MacDiarmid, A. J. Epstein, *Phys. Rev. B* **36**, 3475 (1987); *ibid.* **39**, 3570 (1989).
11. D. Jeon, J. Kim, M. C. Gallagher, R. F. Willis, Y. T. Kim, *J. Vac. Sci. Technol. B* **9**, 1154 (1991).
12. S. Strafström *et al.*, *Phys. Rev. Lett.* **59**, 1464 (1987).
13. E. W. Paul, A. J. Ricco, M. S. Wrighton, *J. Phys. Chem.* **89**, 1441 (1985).
14. H. Kuzmany, N. S. Sariciftci, H. Neugebauer, A. Neckel, *Phys. Rev. Lett.* **60**, 212 (1988).
15. A. G. MacDiarmid, J. C. Chiang, A. F. Richter, A. J. Epstein, *Synth. Met.* **18**, 285 (1987).
16. A. J. Epstein *et al.*, *ibid.*, p. 303.
17. H. H. S. Javadi, K. R. Cromack, M. Angelopoulos, A. G. MacDiarmid, A. J. Epstein, *Phys. Rev. B* **39**, 3579 (1989).
18. J. M. Ginder, A. F. Richter, A. G. MacDiarmid, A. J. Epstein, *Solid State Commun.* **63**, 97 (1987).
19. J. P. Pouget, M. E. Józefowicz, A. J. Epstein, X. Tang, A. G. MacDiarmid, *Macromolecules* **24**, 779 (1991).
20. D. A. Bonnell and M. Angelopoulos, *Synth. Met.* **33**, 301 (1989).
21. R. J. Hamers and R. H. Koch, in *The Physics and Chemistry of SiO_2 and the Si-SiO_2 Interface*, C. Helms and B. Deal, Eds. (Plenum, New York, 1988), p. 201. See also (*11*).
22. For the latest proposal, see R. Garcia, *J. Vac. Sci. Technol. B* **9**, 500 (1991).
23. Also, in the present context, on the height of the barrier and depth of the space-charge region separating the junction from the bulk semiconductor.
24. We thank Y.-T. Kim and K. Vedam for help with preparing the electropolymerized PAN-EB films and R. W. Collins for performing ellipsometry measurements. Supported by NSF grant DMR-8818884 and the Physics Department at Pennsylvania State University (D.J. and J.K.).

10 March 1992; accepted 11 May 1992

Spin Susceptibility Scaling in High-Temperature Superconductors

J. Ruvalds,* C. T. Rieck, J. Zhang, A. Virosztek

The spin response of a nested Fermi surface represented by a tight binding energy band is found to exhibit scaling in frequency divided by temperature within a restricted regime close to half-filling of the band. Computations of the spin susceptibility reveal a surprising momentum variation at various temperatures and frequencies. Neutron scattering data on the high-temperature superconductor $YBa_2Cu_3O_{6+x}$ are analyzed for scaling near a momentum vector that spans nested regions of the orbit. Changes in the Fermi energy remove the scaling properties and reduce the susceptibility to the conventional Fermi liquid behavior of ordinary metals. These results imply that pairing mechanisms of superconductivity need to cope with competing spin density wave and charge density wave instabilities.

The dynamics of electron spins in solids can be described with a susceptibility χ, which in ordinary metals exhibits negligible temperature dependence (*1*). In superconducting copper oxides, however, unusual forms of the spin response are evident in nuclear magnetic resonance (NMR) spectroscopy (*2*) and in neutron scattering studies (*3*). Moreover, small changes in the composition of the cuprates can eliminate the metallic behavior and create an insulating state with antiferromagnetic spin order. It has been proposed that novel spin excitations, including spin polarons (*4*), spin bags (*5*), and spinons (*6*), exist in the cuprates. Hence, understanding spin correlations in the metallic cuprates may provide insight into the mechanism of high-temperature superconductivity.

It is reasonable, therefore, to explore phenomena that could explain the unusual behavior of χ in the cuprates. For example, nesting of Fermi surfaces (*7*), which occurs when sections of an electron orbit in momentum space are nearly parallel, can enhance the electronic susceptibility at a nesting vector $\mathbf{Q}$. This, in turn, may lead to the formation of a spin density wave (SDW) or a charge density wave (CDW) (*8*). A classic example of nesting leads to an SDW in chromium (*9*). These spin and charge instabilities compete with superconductivity, and the corresponding phase diagrams of quasi–one-dimensional systems (*10*) provide relevant examples. In this report, we examine the effects of nesting on spin susceptibility and find an unusual scaling that is in good agreement with recent neutron scattering data.

A representation of nesting by the energy dispersion condition $E(\mathbf{k} + \mathbf{Q}) \cong -E(\mathbf{k})$ provides an analytic solution (*11*) for the lowest order imaginary part of the susceptibility

$$\chi''_0(\mathbf{q},\omega) = -\frac{a^2}{4\pi}\int d^2k \{f[E(\mathbf{k}+\mathbf{q})] - f[E(\mathbf{k})]\}\,\delta[\omega - E(\mathbf{k}+\mathbf{q}) + E(\mathbf{k})] \quad (1)$$

where $f(x) = [\exp(x/T) + 1]^{-1}$ is the Fermi function, and a is the lattice spacing. This ideal approximation allows a straightforward integration over the momentum $\mathbf{k}$ by changing to a variable $x = E(\mathbf{k})$. Thus one obtains

$$\chi''_{NFL}(\mathbf{Q},\omega) \cong \frac{\pi N(0)}{2}\tanh\left(\frac{\omega}{4T}\right) \quad (2)$$

where $N(0)$ is the density of states at the Fermi energy. The variation of this nested Fermi liquid (NFL) response with frequency ω and temperature T is quite different from conventional electron correlations, and the scaling in ω/T is particularly anomalous.

Motivated by the predicted scaling (*11*) and recent neutron scattering probes (*12–18*) of the susceptibility in superconducting crystals of $YBa_2Cu_3O_{6+x}$ and $La_{2-x}Sr_xCuO_4$, we derive limitations on the nesting criteria and find a surprising momentum dependence of the spin correlations on the basis of a tight binding energy band having width $8t$

$$E(\mathbf{k}) = -2t[\cos(ak_x) + \cos(ak_y)] - \mu \quad (3)$$

This model exhibits perfect nesting of a square orbit for a Fermi energy $\mu = 0$ at the nesting vector $\mathbf{Q} = (\pi/a, \pi/a)$. That special case of a half-filled band in two dimensions yields a logarithmic singularity in the density of states and is unstable toward the formation of an SDW for arbitrarily weak Coulomb repulsion. However, lowering μ yields orbits with partial nesting characterized by a wavevector $\mathbf{Q}^* < \mathbf{Q}$ (Fig. 1), and these nesting features resemble the results of sophisticated band structure calculations for the cuprates (*19*, *20*), even though the value of $\mathbf{Q}^*$ may differ.

This model and variations of it that include more terms have been investigated for

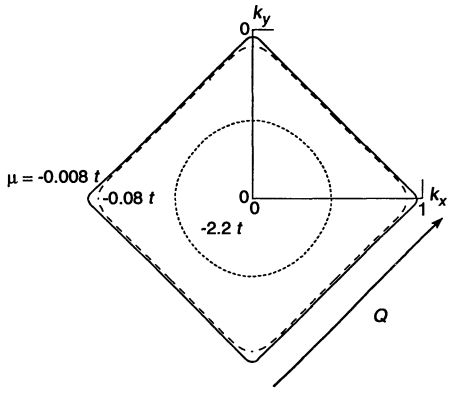

Fig. 1. Fermi surfaces for the model band structure of Eq. 3 are shown for three values of the chemical potential μ. Nearly parallel sections of the electron orbits are spanned by a nesting wave vector $\mathbf{Q}^*$, which is $\mathbf{Q} = (\pi,\pi)/a$ for $\mu = 0$, $\mathbf{Q}^* = 0.999\mathbf{Q}$ for $\mu = -0.008\ t$, and $\mathbf{Q}^* = 0.987\mathbf{Q}$ for $\mu = -0.08\ t$. Scaling of the susceptibility occurs only near half-filling of the band, as in the $\mu = -0.008\ t$ case, and is spoiled by the small curvature of the dashed curve orbit corresponding to $\mu = -0.08\ t$. Conventional Fermi liquid response is found for the nearly spherical orbit shown by the dotted curve with $\mu = -2.2\ t$.

J. Ruvalds, C. T. Rieck, J. Zhang, Physics Department, University of Virginia, Charlottesville, VA 22901.
A. Virosztek, Research Institute for Solid State Physics, 1525 Budapest 114, Post Office Box 49, Hungary.

*New address (effective 15 July 1992): Physics Department, Stanford University, Stanford, CA 94305.

CDW instabilities (*21*) and SDW transitions (*22*) and have been applied to organic superconductors (*23*). Recently it has been used to analyze superconductors whose planar Cu–O structures restrict the electron motion to two dimensions. Numerical calculations of χ have been applied to analysis of the NMR spin relaxation (*24, 25*) and have successfully accounted for (*26–30*) some features of the neutron scattering data including twin peak structure as a function of momentum.

The susceptibility may be related to electrical transport properties, which are anomalous in cuprate superconductors. The observed linear temperature variation of the resistivity has been attributed (*31*) to enhancement of electron-electron scattering by the logarithmic singularity in the density of states that follows from perfect nesting. Nesting of orbit segments also leads to an unconventional linear frequency variation of the electron damping (*11*), and this input explains (*32*) the non-Drude optical reflectivity seen in cuprates.

Numerical calculations of the self-energy of an electron described by models such as Eq. 3 have verified the analytic nesting results (*11*) in nearly half-filled bands, and they also demonstrate a crossover to conventional Fermi liquid response below threshold values of T and ω that are dictated by the orbit topology (*33, 34*).

Our focus here is on the criteria for achieving a scaling in the response function $\chi''(\mathbf{q}, \omega, T)$, using the energy spectrum of Eq. 3. At the vector $\mathbf{Q}$ the susceptibility becomes

$$\chi''(\mathbf{Q},\omega) = \frac{\pi N(\omega/2)}{4}\left[\tanh\left(\frac{\omega - 2\mu}{4T}\right) + \tanh\left(\frac{\omega + 2\mu}{4T}\right)\right] \quad (4)$$

When $\mu = 0$, this function is singular at $\omega = 0$ because the electron velocity at the corners of the corresponding square orbit vanishes and thus generates a logarithmic singularity in the density of states $N(\omega)$. For $\mu = 0$ the system is unstable (*21, 22*) toward formation of a CDW or SDW for arbitrarily weak coupling. Away from half-filling, the form of Eq. 4 is reminiscent of the charge response in CDW studies (*21*) and has also been proposed (*26*) as a kinematical source of spin pseudogap structure in the susceptibility for $\omega < 2\mu$.

For general values of the momentum $\mathbf{q}$, the δ-function integration in Eq. 1 yields

$$\chi_0''(\mathbf{q},\omega) = \frac{-a}{16\pi t|\sin(aq_y/2)|}\int dk_x \sum_i \frac{1}{|\cos(ak_{i,yo} + aq_y/2)|}\{f[E(k_x + q_x, k_{i,yo} + q_y)] - f[E(k_x, k_{i,yo})]\} \quad (5)$$

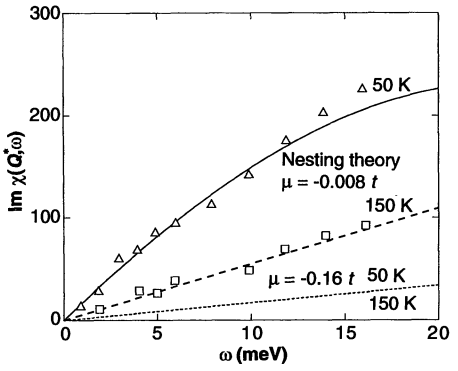

Fig. 2. The unconventional temperature variation of the imaginary part of the susceptibility is demonstrated by the nesting calculation with $\mu = -0.008\ t$ and the neutron scattering data (triangles and squares) on superconducting $YBa_2Cu_3O_{6.5}$ from (*12*). Scaling of the response in ω/T is most evident near the nesting vector $\mathbf{Q}^* \cong \mathbf{Q}$. A standard temperature-independent response in the case of $\mu = -0.16\ t$ appears in the calculated dotted curve, which is essentially the same for $T = 50$ and 150 K. The solid (50 K) and dashed (150 K) calculated curves use $\mu = -0.008\ t$ and $J = 0.24\ t$, which enhances the magnitude of the RPA response, even though the overall frequency and temperature variation resembles the formula of Eq. 2 derived with a nesting condition in the lowest order approximation. The susceptibility is shown in arbitrary units.

Here $ak_{1,yo} = \arcsin(z) - aq_y/2$, $ak_{2,yo} = \pi - \arcsin(z) - aq_y/2$, and

$$z = \{\cos[a(k_x + q_x)] - \cos(ak_x) + \omega/2t\}/2\sin(aq_y/2) \quad (6)$$

For $z < 0$, $ak_{2,yo}$ is constrained to $[-\pi, \pi]$ by choosing the proper arc sin quadrant.

The remaining integration in Eq. 5 is achieved with a numerical routine. The real part of the susceptibility is obtained via a Kramers-Kronig transform:

$$\chi_0'(\mathbf{q},\omega) = \frac{1}{\pi} P \int_{-8t}^{8t} \frac{\chi_0''(\mathbf{q},\omega')d\omega'}{\omega - \omega'} \quad (7)$$

Finally, spin fluctuations within the random phase approximation (RPA) (*1*) give

$$\chi''_{RPA}(\mathbf{q},\omega) = \frac{\chi_0''(\mathbf{q},\omega)}{\left[1 - J\chi_0'(\mathbf{q},\omega)\right]^2 + \left[J\chi_0''(\mathbf{q},\omega)\right]^2} \quad (8)$$

where the effective Coulomb coupling J is estimated from the analysis of the neutron data.

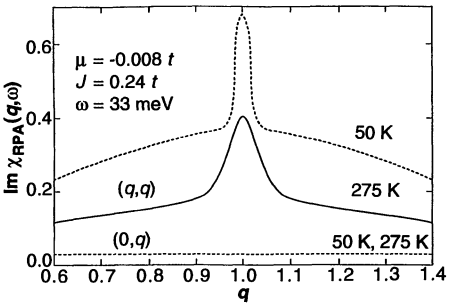

Fig. 3. The calculated momentum dependence of the susceptibility reveals a peak near the nesting vector $\mathbf{Q}^* \cong \mathbf{Q}$, and a surprising temperature variation of the peak width and wings along the (q,q) direction. The 50 K dashed curve shows only a rough overall scaling with the solid curve obtained at 275 K. Along the $(0,q)$ direction that does not intercept the nesting vector $\mathbf{Q}$, the calculated dotted curve is small by comparison and is essentially the same for both 50 and 275 K. The susceptibility is drawn in arbitrary units.

The calculated susceptibility reveals an anomalous temperature variation for a Fermi energy $\mu = -0.008\ t$ as seen in Fig. 2. At the nesting vector $\mathbf{Q}^* \cong \mathbf{Q}$ the frequency variation of χ'' is similar to the NFL prediction of Eq. 2 and is in good agreement with the neutron scattering data (*12*) on $YBa_2Cu_3O_{6.5}$ found at $T = 50$ and 150 K for a value of $J = 0.24\ t$. Scaling on an ω/T plot brings the calculated solid curve (and data triangles) obtained at 50 K into coincidence with the dashed curve (and data squares) obtained at 150 K. The superconducting transition temperature of this sample is $T_c = 47$ K.

Conventional Fermi liquid behavior in

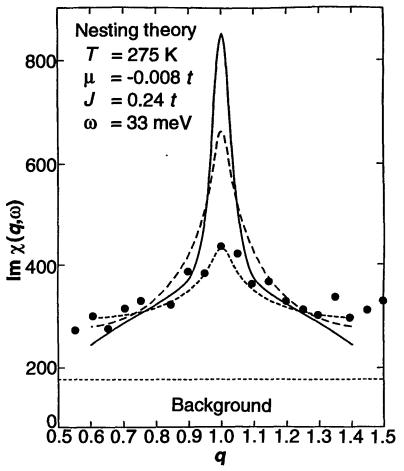

Fig. 4. Comparison of the calculated momentum variation of the susceptibility along the (q, q) direction with the neutron data of (*17*) (points) on $YBa_2Cu_3O_{6.5}$ demonstrates the peak structure near the nesting vector $\mathbf{Q}^* \cong \mathbf{Q}$. The solid curve represents the RPA susceptibility from Eq. 8 using $J = 0.24\ t$ and Fermi energy $\mu = -0.008\ t$. The dashed curve includes a self-energy $\Sigma''_{NFL} = -0.5\ \omega$ at $\omega = 33$ meV and neglects RPA corrections: This broader curve fits the experimental points if the background is as shown, and the calculated peak height magnitude (dotted curve) is varied to match the measured maximum.

the form of a temperature-independent susceptibility appears in the present tight binding model already at a Fermi energy $\mu = -0.16\ t$ as seen for the calculated dotted curve in Fig. 2, which is essentially the same for $T = 50$ and 150 K: Here the nesting vector $\mathbf{Q}^* = 0.971\ \mathbf{Q}$ is not far from the ideal value, and yet the scaling in ω/T is spoiled.

A surprising momentum variation of the calculated susceptibility close to half-filling is shown in Fig. 3 for a fixed frequency $\omega = 33$ meV. Along the $(0,q)$ direction χ'' is small, essentially identical for $T = 50$ and 275 K, and is independent of momentum. However, the scan along (q,q) reveals a peak centered at the ideal nesting vector $\mathbf{Q}$ with a width that increases significantly as the temperature is increased from 50 to 275 K. A peculiar temperature variation of $\chi''(q,q)$ is seen for the calculated solid and dashed curves for all values of q in this direction when self-energy corrections are neglected.

Single-peak structure in $YBa_2Cu_3O_{6.5}$ neutron data (*17*) is compared to the calculated spectrum in Fig. 4. The solid curve obtained from Eqs. 5, 7, and 8 shows a narrow peak centered at the nesting vector $\mathbf{Q}$. A fundamental broadening of this peak is caused by electron self-energy corrections, which we included in an independent calculation using the NFL frequency-dependent damping (*11*) $\Sigma''_{NFL} \cong -0.5\ \omega$, in a generalization of Eq. 1. Thus we find the lowest order susceptibility (with $J = 0$) shown by the dashed line in Fig. 4, which agrees with the neutron spectrum (*17*) when a background intensity at the level shown is included (dotted curve). Despite uncertainties in the experimental resolution and higher order corrections to the theory, the key features of a narrow peak in the susceptibility at the $\mathbf{Q}$ nesting vector and negligible neutron cross sections in other momentum regions are verified by these experiments. For $\omega = 33$ meV the self-energy corrections reduce the temperature dependence of the peak width in agreement with the data (*17*) whereas diminished damping at lower frequencies should allow a substantial peak narrowing at lower temperatures as seen recently in $La_{1.85}Sr_{0.15}CuO_4$ (*16*). Increasing oxygen content should move the Fermi energy farther from half-filling and then twin peaks near the nesting vector $\mathbf{Q}$ are expected to evolve from the orbit topology shown in Fig. 1. The data (*35*) on $YBa_2Cu_3O_{6.6}$ provide indications of peak splitting. Although further detailed structure is seen near 10 meV in the $YBa_2Cu_3O_{6.6}$ data from Brookhaven (*35*), their most recent results confirm the universal behavior of χ'' on the scaling ratio ω/T, which breaks down at very low ω and T. The nesting condition should be violated at low (T,ω), and thus the observed drop in the susceptibility (*35*) may indicate a crossover to conventional Fermi liquid dynamics.

Twin-peak structure was found in earlier calculations (*26, 27, 29*) on tight binding energy band models with $|\mu|$ values larger than the one used here for the scaling analysis. The neutron data (*15*) on $La_{2-x}Sr_xCuO_4$ show well-separated double-peak structure as a function of momentum. Remarkably, scaling of the spin response is found in $La_{1.94}Sr_{0.04}CuO_4$ as well as in the heavily doped case of $x = 0.15$ (*16*). The evolution of nesting as a function of doping poses a challenge to band structure calculations, which invariably predict substantial nesting in the cuprate compositions studied so far (*19, 20*).

The original hypothesis of scaling of the charge susceptibility at very low momenta q was surmised from the anomalous flat electronic Raman spectrum of the high-T_c superconductors as a basis for the "marginal" Fermi liquid (MFL) hypothesis (*36*). However, computation of the response at small q for the energy band model of Eq. 3 yields a susceptibility that is extremely small (proportional to q^2) and that has a frequency variation quite different from the MFL assumption. Alternate explanations of the Raman data include scattering by energy density fluctuations in a Mott-Hubbard system (*37*) and a theory based on an NFL (*38*).

The structure of the scaled response in Eq. 2 will generate a quasi-particle damping from electron-electron collisions that is proportional to frequency and also is linear in temperature in the static limit providing that the nesting momentum region dominates the scattering (*11*). The present results reveal a momentum range that shows the scaling behavior, and the overall intensity of the dominant peaks in the neutron spectra (*17*) follows the scaling behavior that provides a plausible explanation for the abnormal electrical transport in the cuprates above T_c.

The existence of a Fermi surface has been challenged in view of the MFL effective mass singularity $m^* \sim \ln(\omega)$ which results from quasi-particle scattering by excitations whose response exhibits scaling structure (*36*). However, if nesting is the source of the anomalous damping and corresponding effective mass renormalization, there will be a crossover temperature T^* and frequency ω^* below which the nesting condition is not satisfied and the Fermi surface is well defined.

A constraint on our analysis is the value of J that we estimate to be an order of magnitude smaller than the bandwidth to avoid an unphysical SDW transition. The tendency to form SDW structures will be reduced by smaller nesting segments as seen in band structure calculations (*19, 20*), by screening of the Coulomb repulsion, by energy band anisotropy, and by impurities. Similar influences apply to CDW instabilities that would be favored by strong electron-phonon coupling (*21*). Nevertheless, these CDW and SDW instabilities will compete with mechanisms of superconductivity that invoke pairing of charge carriers.

The neutron scattering cross sections shown in Figs. 2 and 4 are much different from expectations for localized spins. If the oxygen content is lowered in $YBa_2Cu_3O_{6+x}$, the present model would indicate more complete nesting with a transition to an SDW state. However, the value of the corresponding energy gap and other features of the metal-insulator transition require study beyond the scope of the present analysis.

A puzzling feature in band structure results for $YBa_2Cu_3O_7$ is a rotation of the Fermi surface and the nesting vector $\mathbf{Q}^*$ by 45° with respect to the orbits shown in Fig. 1. Yet the neutron data on the oxygen-depleted crystals demonstrate strong scattering near the nesting vector $\mathbf{Q}$, which is appropriate for Fig. 1. A possible resolution of this dilemma may be a momentum-dependent $J(\mathbf{q})$ (*27*). Nevertheless, a microscopic description of the energy band evolution as a function of oxygen content poses a fundamental challenge for theory and future experimental probes.

The present explanation of the momentum and frequency variation of the superconducting cuprate neutron spectra at various temperatures contains analogies to the itinerant electron antiferromagnetism in chromium. Thus, it is reassuring that various similarities are observed in the neutron spectra (*39*) of chromium and its alloys.

REFERENCES AND NOTES

1. D. Pines and P. Nozieres, *The Theory of Quantum Liquids* (Benjamin, Elmsford, NY, 1966).
2. R. E. Walstedt and W. W. Warren, Jr., *Science* **248**, 1082 (1990).
3. R. J. Birgeneau and G. Shirane, in *Physical Properties of High Temperature Superconductors*, D. M. Ginsberg, Ed. (World Scientific, Singapore, 1989), p. 151.
4. N. F. Mott, *Adv. Phys.* **39**, 55 (1990).
5. A. Kampf and J. R. Schrieffer, *Phys. Rev. B* **41**, 6399 (1990).
6. P. W. Anderson, *Science* **235**, 1196 (1987).
7. W. M. Lomer, *Proc. Phys. Soc. London* **80**, 489 (1962).
8. A. W. Overhauser, *Phys. Rev.* **128**, 1437 (1962).
9. E. Fawcett, *Rev. Mod. Phys.* **60**, 209 (1988).
10. H. Gutfreund and W. A. Little, in *Highly Conducting One Dimensional Solids*, J. T. Devreese *et al.*, Eds. (Plenum, New York, 1979), p. 305.
11. A. Virosztek and J. Ruvalds, *Phys. Rev. B* **42**, 4064 (1990).
12. J. Rossat-Mignod *et al.*, *Physica B* **169**, 58 (1991).
13. J. M. Tranquada *et al.*, *Phys. Rev. Lett.* **64**, 800 (1990).
14. G. Shirane *et al.*, *ibid.* **63**, 330 (1989).
15. S. W. Cheong *et al.*, *ibid.* **67**, 1791 (1991).
16. R. Keimer *et al.*, *ibid.*, p. 1930; T. R. Thurston *et al.*, in preparation.
17. R. J. Birgeneau *et al.*, *Z. Phys. B* **87**, 1 (1992).

18. P. Bourges *et al.*, *Phys. Rev. B* **43**, 8690 (1991).
19. See, for example, J. Yu, A. J. Freeman, J. H. Xu, *Phys. Rev. Lett.* **58**, 1035 (1987); J. Yu *et al.*, *Phys. Lett. A* **122**, 203 (1987).
20. W. E. Pickett, *Rev. Mod. Phys.* **61**, 433 (1989); *Phys. Rev. B* **42**, 8764 (1990); ———, H. Krakauer, R. E. Cohen, D. J. Singh, *Science* **255**, 46 (1992).
21. C. A. Balseiro and L. M. Falicov, *Phys. Rev. B* **20**, 4457 (1979).
22. Y. Hasegawa and H. Fukuyama, *Jpn. J. Appl. Phys.* **26**, L322 (1987).
23. T. Ishiguro and K. Yamaji, *Organic Superconductors* (Springer-Verlag, Berlin, 1990).
24. N. Bulut, D. Hone, D. J. Scalapino, N. E. Bickers, *Phys. Rev. Lett.* **64**, 2723 (1990); *Phys. Rev. B* **41**, 1797 (1990).
25. J. P. Lu, Q. M. Si, J. H. Kim, K. Levin, *Phys. Rev. Lett.* **65**, 2466 (1990).
26. N. Bulut, in *Dynamics of Magnetic Fluctuations in High-Temperature Superconductors*, G. Reiter, Ed. (Plenum, New York, 1990), p. 97, and references cited therein.
27. J. P. Lu, Q. M. Si, J. H. Kim, K. Levin, *Physica C* **179**, 191 (1991).
28. S. V. Maleyev, *J. Phys. I (France)* **2**, 181 (1992).
29. N. Bulut and D. J. Scalapino, *Phys. Rev. Lett.* **68**, 706 (1992); *Phys. Rev. B* **45**, 2371 (1992).
30. T. Tanamoto, K. Kuboki, H. Fukuyama, *J. Phys. Soc. Jpn.* **60**, 3072 (1991).
31. P. A. Lee and N. Read, *Phys. Rev. Lett.* **58**, 2691 (1987).
32. J. Ruvalds and A. Virosztek, *Phys. Rev. B* **43**, 5498 (1991).
33. S. Wermbter and L. Tewordt, *ibid.*, p. 10530.
34. J. W. Serene and D. W. Hess, *ibid.* **44**, 3391 (1991).
35. J. M. Tranquada *et al.*, in preparation; B. J. Sternlieb *et al.*, in preparation.
36. C. M. Varma *et al.*, *Phys. Rev. Lett.* **63**, 1996 (1989); G. Kotliar *et al.*, *Europhys. Lett.* **15**, 655 (1991).
37. B. S. Shastry and B. I. Shraiman, *Phys. Rev. Lett.* **65**, 1068 (1990).
38. A. Virosztek and J. Ruvalds, *ibid.* **67**, 1657 (1991).
39. B. H. Grier, G. Shirane, S. A. Werner, *Phys. Rev. B* **31**, 2892 (1985); E. Fawcett, S. A. Werner, A. Goldman, G. Shirane, *Phys. Rev. Lett.* **61**, 558 (1988).
40. We appreciate helpful information from H. Monien, G. Aeppli, M. Kastner, and J. M. Tranquada. This research was supported by Department of Energy grant DE-FG05-84ER45113 and by Hungarian National Research Fund grants OTKA 2950 and T4473.

26 February 1992; accepted 27 April 1992

Soluble Aluminum Silicates: Stoichiometry, Stability, and Implications for Environmental Geochemistry

B. A. Browne and C. T. Driscoll

Soluble aluminum silicate (Al-Si) complexes are critical species for the development and application of geochemical models. A fluorescence probe technique was used to show that Al-Si complexes account for up to 95% of the total inorganic mononuclear Al in natural waters. The presence of these soluble Al-Si species affects the solubility of Al-Si minerals. Soluble Al-Si species may be important intermediates in the weathering reactions of primary Al-Si minerals and should be considered in dissolution models. Soluble Al-Si species may be key components controlling the formation of metastable and new stable minerals during interactions between water and rocks or soils.

Despite an abundance of Al and H-silicate (H_4SiO_4) ions in natural solutions in contact with Al-Si surfaces in soil and geological formations (*1*), little attention has been accorded to soluble Al-Si species. Soluble Al-Si species may be intermediate in the decomposition of activated complexes (*2*) formed on the surfaces of minerals (for example, potassium-feldspar) during the hydrolytic reaction in aqueous solutions and may play a key role in the formation of metastable and new stable minerals during rock-water and soil-water interactions. Consideration of soluble Al-Si is critical for the development and application of geochemical and soil models. In this report, we characterize the significance and thermodynamic stability of a 1:1:0 Al:Si:OH complex and of 2:2:*r* and 2:1:*r* Al-Si species.

B. A. Browne, School of the Environment, Duke University, Durham, NC 27706.
C. T. Driscoll, Department of Civil and Environmental Engineering, Syracuse University, Syracuse, NY 13244.

We applied a fluorescence probe technique (*3*) to characterize low-order (mononuclear and dinuclear) soluble Al-Si species. Aluminum and Si were combined at low concentrations in dilute acidic solutions of the fluorescence reagent morin (Table 1) (*4*). We measured concentrations of Al^{3+} and total silicate-bound Al (Al-Si) by comparing the fluorescence signal to that of solutions lacking Si (*4*). Because the Al-morin complexes give a large fluorescence signal, the fraction of total soluble Al responsible for the fluorescence signal can be maintained at a low value (typically less than 10%) in the analysis. The method is thus sensitive to subtle differences in the equilibrium distribution of soluble Al, an outcome that has not been achieved with other methods for the analysis of Al. Stability constants for aqueous aluminum fluoride and aluminum sulfate complexes measured by the morin technique compare favorably to published values (*4*).

We evaluated the stoichiometry of Al-Si according to the following reaction series, allowing for the formation of mixed hydroxy-Al-silicates:

$$pAl^{3+} + qH_4SiO_4 + rH_2O = Al_p(OH)_r(OSi(OH)_3)_q^{3p-q-r} + (q + r)H^+ \quad (1)$$

where p, q, and r are stoichiometric coefficients. From Eq. 1, the equilibrium concentration of the pqrth complex is given by:

$$[Al_p(OH)_r(OSi(OH)_3)_q^{3p-q-r}] = K_{pqr}(\tau_3/\tau_{3p-q-r})[Al^{3+}]^p[H_4SiO_4]^q\{H^+\}^{-(q+r)} \quad (2)$$

where K_{pqr} is the equilibrium constant for the pqrth complex, brackets signify concentration, braces signify activity, and τ_i symbolizes the activity coefficient for an Al species. The total concentration of Al-Si at equilibrium may be described in terms of measured reaction variables ($[Al^{3+}]$, $[H_4SiO_4]$, and $\{H^+\}$):

$$[\text{Al-Si}] = \sum_1^P \sum_1^Q \sum_0^R pK_{pqr}(\tau_3/\tau_{3p-q-r})[Al^{3+}]^p[H_4SiO_4]^q\{H^+\}^{-(q+r)} \quad (3)$$

Table 1. Summary of maximum stoichiometric coefficients (Eq. 4) for Al (P), Si (Q), and H_2O (R) observed in the experiments (25° ± 0.1°C, 0.01 M ionic strength, 0.001 M CH_3COO^-, 1 μM total morin) and proposed stoichiometries of Al-Si species. n is the number of samples.

n	pH	H_4SiO_4 (mM)	Total Al (μM)	Maximum stoichiometric coefficient			Proposed species stoichiometries (p,q,r^*)
				P	Q	R	
16	4.0	0.10	0.64–10.3	1	1	0	1,1,0
16	4.0	0.26	0.64–10.3	1	1	0	1,1,0
16	4.5	0.10	0.64–10.3	1	1	0	1,1,0
16	4.5	0.27	0.64–10.3	1	1	0	1,1,0
32	5.0	0.11	0.64–10.3	1	1	0	1,1,0
13	5.5	0.11	0.26–4.07	2	2	2*	1,1,0; 2,1,2*; 2,2,2*
13	5.5	0.25	0.26–4.07	2	2	2*	1,1,0; 2,1,2*; 2,2,2*

*Based on 2:1:2 and 2:2:2 Al:Si:OH mineral analogs imogolite and allophane.